NOAA Technical Memorandum ERL WPL-227

THEORY AND PERFORMANCE OF THE WPL CROSSWIND PROFILER MODEL II

G. R. Ochs
R. J. Lataitis
J. J. Wilson

noaa NATIONAL OCEANIC AND ATMOSPHERIC ADMINISTRATION / Environmental Research Laboratories
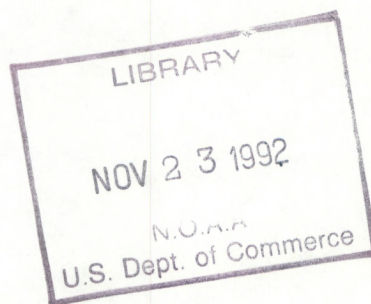
NOAA Technical Memorandum ERL WPL-227

THEORY AND PERFORMANCE OF THE WPL CROSSWIND PROFILER MODEL II

G. R. Ochs
R. J. Lataitis
J. J. Wilson

Wave Propagation Laboratory
Boulder, Colorado
September 1992

NOTICE

Mention of a commercial company or product does not constitute an endorsement by the NOAA Environmental Research Laboratories. Use of information from this publication concerning proprietary products or the tests of such products for publicity or advertising purposes is not authorized.

TABLE OF CONTENTS

THEORY AND PERFORMANCE OF THE WPL
CROSSWIND PROFILER MODEL II

G. R. Ochs[1], R. J. Lataitis[2], and J. J. Wilson[2]

ABSTRACT

A system that measures the crosswind component at five locations along an optical path has been developed. The theory of operation is discussed, and wind data from the operation of the system on a 500-m path agrees well with that predicted by the theoretical analysis.

1. INTRODUCTION

Various optical systems have been proposed and implemented that use the drifting of the intensity scintillation of a light source, as seen at a receiver, to measure the transverse wind component at right angles to the line of sight (Lawrence et al., 1972; Ochs and Miller, 1973; Wang et al., 1974; Clifford et al., 1975; Ochs et al., 1976a; Ochs and Wang, 1978; Ochs and Cartwright, 1980). Over a period of years, improved techniques for obtaining wind measurements from the scintillation have been developed. Initially, laser light sources were used (Lawrence et al., 1972; Ochs and Miller, 1973; Wang et al., 1974). The saturation of scintillation affected the wind measurement on paths having high integrated turbulence, however. These effects were minimized by using large incoherent light sources and receivers (Ochs et al., 1976a). Quartz-halogen incandescent light sources were first used. These light sources were later replaced with light-emitting diodes (LEDs) when high power versions became available (Ochs and Cartwright, 1980). Though the LEDs radiate less total power, the radiation is over a much narrower bandwidth and is easily modulated, so that by using the LEDs, the overall signal-to-noise ratio is improved. The methods of analyzing the signals to obtain wind speed have also evolved over this period, and the latest techniques measure more accurately by using more of the information contained in the scintillation pattern (Wang et al., 1981).

It is possible, by changing the transmitter or receiver optics, to measure the crosswind over only portions of the optical path. In fact, the instruments that measure a so-called space-averaged crosswind respond most strongly to winds in the central one-third of the optical path, tapering to zero response at the transmitter and receiver; i.e., the weighting of

---

[1]Science and Technology Corporation, 3100 Arapahoe Ave., Boulder, CO 80303.

[2]Wave Propagation Laboratory, NOAA/ERL, 325 Broadway, Boulder, CO 80303.

the response is a bell-shaped curve. With incoherent aperture systems, this weighting function can be biased toward one end of the path by making the aperture diameter smaller at that end. A system using this principle has been analyzed and constructed (Ochs and Wang, 1978). To obtain sharper weighting functions, however, more complex transmitting and receiving filters are required.

The Crosswind Profiler Model II that is analyzed and described here is based on a technique first proposed by Lee (1974), and was developed by the Wave Propagation Laboratory (WPL) of NOAA. Four prototype units were constructed. A detailed description of the system is contained in NOAA Technical Memorandum ERL WPL-152 (Ochs et al., 1988). In this companion report we develop the equations that predict system performance, and describe the results of experiments designed to measure the actual performance of the system. Additional measurements of system performance are described by Bilthoft (1988) and Wang and Bilthoft (1991). A commercial version that also profiles refractive-index turbulence (C_n^2) is now available.[*]

2. ANALYSIS

Lee (1974) initially described a line-of-sight technique in which spatial filters were used to obtain highly localized measurements of atmospheric turbulence. The method required an extended, spatially incoherent source and receiver with spatially modulated aperture responses. This spatial modulation could be generated, for example, by placing vertically striped transmission masks across the transmitting and receiving apertures. The stripes alternately block and pass the incident light. The resulting transmission functions are 1 everywhere the light is passed and 0 everywhere it is blocked. They are characterized by their spatial wavelengths, Λ_t and Λ_r, which, in this example, are the distances between the centers of the stripes that form the filters. This modulation filters spatially the optical scintillation pattern produced when light passes through a random medium such as the atmosphere. It is also possible to construct a system with more complicated "zero-sum" filters that have transmission functions which oscillate about 0. We discuss in detail how this is accomplished later in this section. Lee (1974) demonstrated that such a system was sensitive to the transverse motion of refractive index irregularities only at the single path position:

$$z_0 = L \frac{K_r}{K_r + K_t} = L \frac{1}{1 + \dfrac{\Lambda_r}{\Lambda_t}} \,, \tag{1a}$$

where L is the propagation path length, and $K_t = 2\pi/\Lambda_t$ and $K_r = 2\pi/\Lambda_r$ are the spatial wavenumbers of the transmitter and receiver filters, respectively. In addition, he showed that such a system was sensitive only to the single scale size $\Lambda_0 = 2\pi/K_0$ of the irregularities at z_0, where

$$K_0 = |\vec{K}_0| = |\vec{K}_t + \vec{K}_r| . \tag{1b}$$

The vector nature of the wavevectors $\vec{K}_t$ and $\vec{K}_r$ in (1b) describes the orientation of the spatial filters. A vertically striped filter would, for example, have a wavevector pointed horizontally, although there would still remain an inconsequential ambiguity in sign. In (1b), we have assumed that the transmitter and receiver filters always have the same orientation; that is, $\vec{K}_t$ and $\vec{K}_r$ point in the same direction.

Lee (1974) showed that the variance of the spatially filtered intensity fluctuations was proportional to the turbulence intensity described by the refractive index structure parameter C_n^2 at the single path position z_0. He also indicated that the angular frequency ω_0 of the filtered fluctuations was related to the transverse wind velocity $\vec{V}$ at z_0 through $\omega_0 = [\vec{K}_0 \cdot \vec{V}(z_0)]$, so that the component of the wind velocity along $\vec{K}_0$ could be measured. With vertically striped filters we could, for example, measure the horizontal wind. Clearly, by changing Λ_t or Λ_r, different path positions could be probed and profiles of C_n^2 and the transverse wind along a line-of-sight propagation path retrieved. The resolution Δ of such a system, in percent of the total path length, is typically (Churnside et al., 1988) $64/(N_t + N_r)$, where N_t and $N_r \gg 1$ are the number of spatial cycles in the transmitter and receiver filters, respectively. We caution, however, that this estimate is based on a highly idealized model for the spatial filters and should be considered only as an approximate measure of the resolution.

A substantial amount of recent theoretical and experimental work on this technique (Churnside et al., 1988; Ochs et al., 1976b; Hill, 1982; Lataitis et al., 1986; Clifford and Churnside, 1987; Clifford and Lataitis, 1987) demonstrates its tremendous potential for obtaining high-resolution turbulence measurements. This report describes for the first time the potential performance of a practical wind profiling system based on the spatial filter concept.

We first consider the transmitter and receiver filters, shown in Figs. 1 and 2, respectively. Two transmitter filters with $\Lambda_t = 20$ cm and 5 cm are used in the system. The filters are zero-sum; that is, the detected light intensity from the elements labeled "-" is subtracted from the detected light intensity from the elements labeled "+". This is accomplished by coding the signals from the different regions of the transmitter so that they can be uniquely identified at the receiver. The three receiver filters (Fig. 2) have spatial wavelengths of $\Lambda_r = 20$ cm, 10 cm, and 5 cm. They are also zero-sum in that light detected by the elements marked "-" is subtracted from that detected by those labeled "+". The receiver filters have spaces between the elements to allow for a second identical filter shifted in space by $\Lambda_r/4$ needed to identify the wind direction. With this system we can probe the horizontal component V_x of the wind at five different path positions, one for each transmitter-receiver pair

combination (except for two combinations that give the same result). The different normalized path positions $u_0 = z_0/L = [1 + (\Lambda_r/\Lambda_t)]^{-1}$ and spatial wavelengths $\Lambda_0 = 2\pi/K_0 = \Lambda_t\Lambda_r/(\Lambda_t + \Lambda_r)$ sampled are shown in Table 1 along with the number of spatial cycles N_t and N_r across the transmitter and receiver filters, respectively, and the expected path resolution Δ. We note that the frequency f_0 of the spatially filtered intensity and the horizontal component $V_x(u_0)$ of the wind are related through $f_0 = V_x(u_0)/\Lambda_0$.
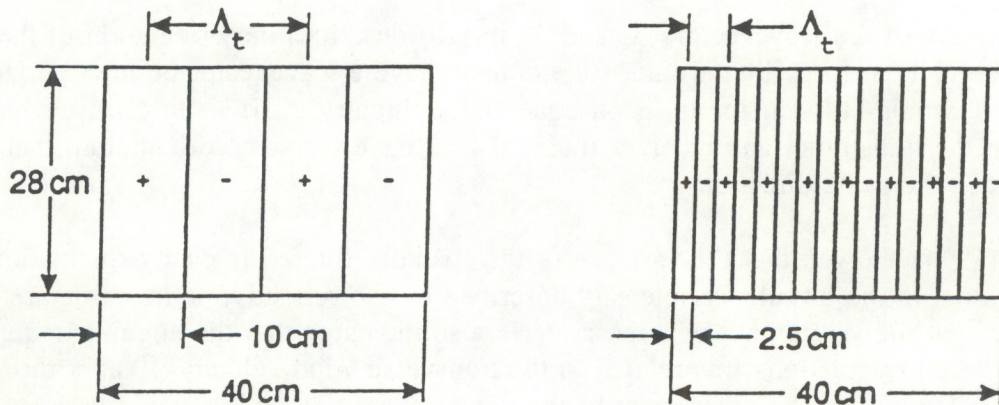
Figure 1. A schematic of the two spatial-filter transmitters used in the system. The corresponding spatial wavelengths (Λ_t) are 20 cm and 5 cm. The "+" and "-" signs identify regions of the transmitter aperture from which the detected light intensity is either weighted by +1 or -1, respectively, before the contributions from all of the transmitting elements are summed.

Figure 2. A schematic of the three spatial-filter receivers used in the system. The corresponding spatial wavelengths (Λ_r) are 20 cm, 10 cm, and 5 cm. The "+" and "-" signs identify regions of the receiver aperture from which the detected light intensity is either weighted by +1 or -1, respectively, before the contributions from all of the receiving elements are summed.
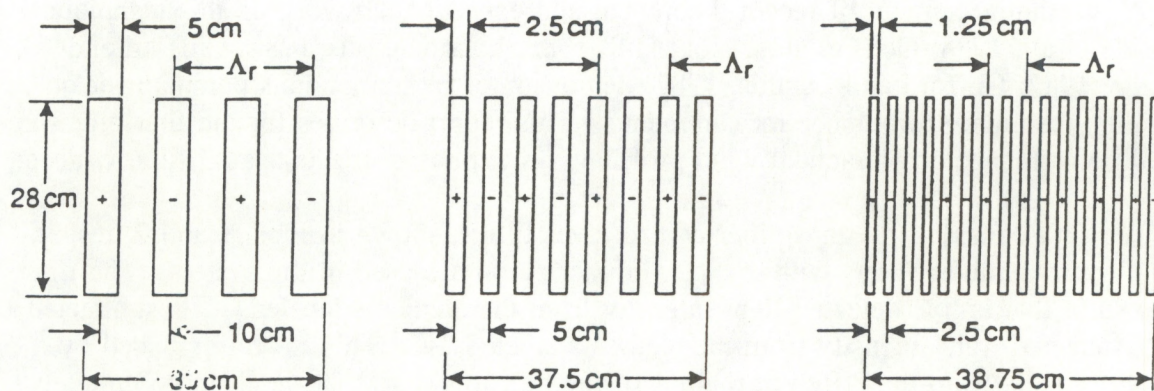
4

Table 1. The spatial wavelengths of the transmitter (Λ_t) and receiver (Λ_r) filters in Fig. 1, together with the expected spatial scale $\Lambda_0 = K_0/2\pi$ and normalized path position $u_0 = z_0/L$, sampled as computed from (1a) and (1b), respectively. The number of spatial cycles in the transmitter filter N_t and receiver filter N_r, and the expected path resolution $\Delta \sim 64/(N_t + N_r)$ are also shown.

Λ_t (cm)	Λ_r (cm)	Λ_0 (cm)	u_0	N_t	N_r	Δ (%)
20	5	4.00	0.80	1.5	7.5	7.11
20	10	6.67	0.67	1.5	3.5	12.8
20	20	10.0	0.50	1.5	1.5	21.3
5	5	2.50	0.50	7.5	7.5	4.27
5	10	3.33	0.33	7.5	3.5	5.82
5	20	4.00	0.20	7.5	1.5	7.11

The values for u_0 and Λ_0 shown in Table 1 are based on geometric optics arguments and on the assumption that the spatial filters are ideal; that is, they have an infinite transverse extent and perfectly sinusoidal character. Clearly, the filters shown in Fig. 1 only approximate the ideal case, and it is therefore important to compute their actual path and wavenumber response.

Wind information is obtained from the time-delayed covariance of signals from two spatial filter receivers shifted in space by $\Lambda_r/4$. The mean frequency of the covariance reflects the wind speed, and the sign of the delay to the peak, or sign of the slope at zero-lag, reflects the wind direction (Wang et al., 1981). The equation for the spatially filtered space-time intensity covariance $C_f(\vec{\rho}, \tau)$, where $\vec{\rho}$ is the transverse vector separation of the two receiving filters and τ is the time delay, is given by (Clifford and Churnside, 1987)

$$C_f(\vec{\rho}, \tau) = 8\pi k^2 L \int_0^1 du \int d^2\vec{K} \; \Phi_n(\vec{K}, 0, u) \, e^{i\vec{K} \cdot [\vec{\rho}u + \vec{V}(u)\tau]}$$

$$\times \sin^2\left[K^2 \frac{Lu(1-u)}{2k}\right] \; |F_t[\vec{K}(1-u)]|^2 \; |F_r(\vec{K}u)|^2 , \tag{2a}$$

where $k = 2\pi/\lambda$, λ is the optical wavelength, $u = z/L$ is the normalized path position, z is the position along the path, and $\Phi_n(\vec{K}, K_z, u)$ is the normalized, path-dependent, three-dimensional refractive index spectrum evaluated at the transverse wave vector $\vec{K}$ and longitudinal wavenumber K_z. The functions $|F_t|^2$ and $|F_r|^2$ are proportional to the spatial power spectra of the transmitter and receiver transmission functions $f_t(\vec{r})$ and $f_r(\vec{r})$, respectively, where $\vec{r}$ is a transverse vector in either the transmitting or receiving plane, and are defined through

$$|F_{t,r}(\vec{\Gamma})|^2 = \frac{1}{A_{t,r}} \int d\vec{r}^{\,2} \, e^{i\vec{\Gamma}\cdot\vec{r}} f_{t,r}(\vec{r}) \, . \tag{2b}$$

In (2b) A_t and A_r are the effective areas of the transmitter and receiver apertures, respectively. Equations (2a) and (2b) are valid provided Taylor's hypothesis holds, the turbulence statistics are stationary and homogeneous, and the turbulence outer scale $L_0 \ll L$ (Tatarskii, 1971).

The quantity described by (2a) and (2b) can be experimentally generated in the following way. The signal S_f from the spatial-filter system is found by taking the signal S_+, obtained by summing the signals from each pair of transmitter-receiver elements of like sign, and subtracting the signal S_-, obtained by summing the signals from each pair of transmitter-receiver elements of the opposite sign; that is, $S_f = S_+ + S_-$. If we take the signal S_f at time t and position $\vec{\rho}_1 + \vec{\rho}$ and form the time-lagged correlation with the signal S_f at time $t + \tau$ and position $\vec{\rho}_1$, and then divide the result by the square of the mean unfiltered signal S (i.e., the detected intensity with all of the "-" elements changed to "+" elements), we obtain $C_f(\vec{\rho},\tau)$ as defined by (2a). That is,

$$C_f(\vec{\rho}, \tau) \approx \frac{\overline{S_f(\vec{\rho}_1 + \vec{\rho}, t)\, S_f(\vec{\rho}_1, t + \tau)}}{\overline{S}^2} \, , \tag{3}$$

where the overbar describes a time average and we have assumed homogeneous and stationary propagation statistics.

For filters with many spatial cycles we expect the fluctuations in the filtered intensity to be narrow band, and the corresponding space-time covariance to be essentially sinusoidal with a frequency $f_0 \sim |V_x(u_0)|/\Lambda_0$. This frequency can be measured in a variety of ways, including counting zero crossings or computing the peak or the mean frequency of the corresponding power spectrum. Each method will have slightly different path and wave-number responses. We choose to base our calculations on the computation of the mean angular frequency $\tilde{\omega}$ of the space-time covariance function. This can be found by first computing the spatially filtered cospectrum $S_f(\vec{\rho}, \omega)$ defined by

6

$$S_f(\vec{\rho}, \omega) = \frac{1}{2\pi} \int_{-\infty}^{\infty} d\tau \, C_f(\vec{\rho}, \tau) \, e^{-i\omega\tau} . \tag{4}$$

Substituting (2a) in (4), assuming the transverse wind vector $\vec{V}(u)$ has only a component $V_x(u)$ in the horizontal, and the separation $\vec{\rho}$ of the spatial filter receivers is a distance ρ_x in the horizontal, we obtain

$$S_f(\rho_x, \omega) = 8\pi k^2 L \int_0^1 du \int_{-\infty}^{\infty} dK_x \, \delta[\omega - K_x V_x(u)] \int_{-\infty}^{\infty} dK_y \, \Phi_n(K_x, K_y, 0, u)$$

$$\times \, e^{iK_x\rho_x u} \, \sin^2\left[\frac{(K_x^2 + K_x^2) \, Lu(1-u)}{2k} \right] |F_t[K_x(1-u), K_y(1-u)]|^2 \, |F_r(K_x u, K_y u)|^2 ,$$

$$\tag{5}$$

where δ is the Dirac delta function. Using (5) to compute the mean angular frequency (see Appendix), we obtain

$$\tilde{\omega} \approx \frac{Im\left\{ \int_0^{\infty} d\omega \, \omega \, S_f(\rho_x, \omega) \right\}}{Im\left\{ \int_0^{\infty} d\omega \, S_f(\rho_x, \omega) \right\}} \tag{6a}$$

$$= K_{x0} \int_0^1 du \, |V_x(u)| \, W_N(u) , \tag{6b}$$

where K_{x0} is the sampled horizontal wavenumber as computed by (1b),

$$W_N(u) = \frac{W(u)}{\int_0^1 du \, W'(u)} \tag{6c}$$

$$W(u) = 16\pi k^2 L \int_0^\infty dK_x \int_0^\infty dK_y K_x \sin(K_x \rho_x u) \; \Phi_n(K_x, K_y, 0, u)$$

$$\times \sin^2\left[\frac{(K_x^2 + K_y^2)\, Lu(1-u)}{2k} \right] \; |F_t[K_x(1-u), K_y(1-u)]|^2 \; |F_r(K_x u, K_y u)|^2 \qquad (6d)$$

is the path weighting function describing the sensitivity of the mean frequency measurement to the transverse velocity at different parts of the path, K_x and K_y represent the horizontal and vertical components, respectively, of the transverse wavevector $\vec{K}$, and W' is given by (6d) with the K_x factor preceding the **sin** term in the integrand replaced by K_{x0} . We note that the path weighting function calculated in this manner is identical to that obtained by using the slope at zero lag of the covariance to infer the wind speed (Wang et al., 1981). We have assumed in (6d) that $|F_t|^2$ and $|F_r|^2$ are even in K_x and K_y.

To numerically examine the behavior of (6d), we use the Kolmogorov form for the refractive index spectrum (Tatarskii, 1971)

$$\phi_n(K_x, K_y, 0, u) = \frac{0.033\, C_n^2(u)}{(K_x^2 + K_y^2)^{11/6}} \qquad (7)$$

valid in the initial subrange $2\pi/L_0 \ll K \ll 2\pi/l_0$, where l_0 is the turbulence inner scale. We also assume the refractive index structure parameter $C_n^2(u) = C_n^2$ is independent of path position and use the change of variables $x = K_x L_t$ and $y = K_y H_t$, where L_t and H_t are the length and height of the transmitter aperture, to obtain

$$W(u) = 1.66\, k^2 L C_n^2 H_t^{8/3} L_t^{-2} \int_0^\infty dx \int_0^\infty dy \, \frac{x\sin(\alpha x u)}{[(\beta x)^2 + y^2]^{11/6}}$$

$$\times \sin^2\{ [(\delta x)^2 + (\epsilon y)^2]\, u(1-u) \} \left| F_t\left[\frac{x}{L_t}(1-u), \frac{y}{H_t}(1-u) \right] \right|^2$$

$$\times \left| F_r\left(\frac{x}{L_t} u, \frac{y}{H_t} u \right) \right|^2 , \qquad (8)$$

where $\alpha = \rho_x/L_t$, $\beta = H_t/L_t$, $\delta = \sqrt{L/2k}\,/L_t$, and $\epsilon = \sqrt{L/2k}\,/H_t$.

8

F_t and F_r in (8) can be evaluated using (2b). For the transmitter and receiver configurations shown in Figs. 1 and 2, the transmission functions f_t and f_r are 1 everywhere there is a "+" sign, -1 everywhere there is a "-" sign, and 0 elsewhere. The actual computation of F_t and F_r is tedious but straightforward. We find that for the two transmitter configurations

$$F_t\left(\frac{a}{L_t}, \frac{b}{H_t}\right) = \begin{cases} 2\,sinc\left(\frac{b}{2}\right)\frac{1}{a}\left(1 - 2\cos\frac{a}{4} + \cos\frac{a}{2}\right) & \text{(9a)} \\[3mm] 2\,sinc\left(\frac{b}{2}\right)\frac{1}{a}\left(1 + \cos\frac{a}{2} + 2\sum_{n=1}^{7}(-1)^n\cos\frac{an}{16}\right), & \text{(9b)} \end{cases}$$

and for the three receiver configurations,

$$F_r\left(\frac{a}{L_t}, \frac{b}{H_t}\right) = \begin{cases} 2\,sinc\left(\frac{b}{2}\gamma\right)\frac{1}{a}\sum_{n=0}^{3}\left(\cos\frac{n\pi}{2} - \sin\frac{n\pi}{2}\right)\cos\left(a\frac{2n+1}{14}\gamma'\right), & \text{(9c)} \\[3mm] 2\,sinc\left(\frac{b}{2}\gamma\right)\frac{1}{a}\sum_{n=0}^{7}\left(\cos\frac{n\pi}{2} - \sin\frac{n\pi}{2}\right)\cos\left(a\frac{2n+1}{30}\gamma'\right), & \text{(9d)} \\[3mm] 2\,sinc\left(\frac{b}{2}\gamma\right)\frac{1}{a}\sum_{n=0}^{15}\left(\cos\frac{n\pi}{2} - \sin\frac{n\pi}{2}\right)\cos\left(a\frac{2n+1}{62}\gamma'\right), & \text{(9e)} \end{cases}$$

where $\gamma = H_r/H_t$, H_r is the receiver aperture height, $\gamma' = L_r/L_t$, and L_r is the receiver aperture length. Note that L_r is different for the three receiver configurations. $W(u)$ is shown plotted in Fig. 3 on a relative scale for the different transmitter and receiver configurations shown in Figs. 1 and 2 using $L = 1$ km and $\lambda = 0.93\,\mu$m.

Two possible configurations give path weighting functions peaked at $u = 0.5$. The dashed line corresponds to line 3 in Table 1. The peaks in the path weighting functions agree almost exactly with those predicted by (1a). The expected resolution Δ in Table 1, which is roughly the half-power or e^{-1} width of the path weighting function in percent of the total path, agrees fairly well with the predicted result. The discrepancies are due to the spatial filter model used to calculate Δ, which considered only infinite Gaussian apertures and a perfectly sinusoidal modulation.

9

Figure 3. The relative path weight, computed from W(u) defined in (8) and the transmission function defined in (9), is shown plotted as a function of the normalized path position $u = z/L$, where z is the position along a propagation path of length L, for the transmitter and receiver configuration shown in Figs. 1 and 2. A path length $L = 1$ km and a wavelength $\lambda = 0.93$ μm were used in the calculations.

One characteristic of the path weighting functions shown is the presence of sidelobes that may contaminate the measurements. The sidelobes are due to the finite size and the square wave nature of the modulation across the apertures. By making the modulation more sinusoidal, the sidelobes can be significantly suppressed. This can be accomplished by sinusoidally shading the transmitting and receiving apertures, or by using more transmitting and receiving elements and weighting the received signals from each to mimic a sinusoidal response, instead of simply using a +1 or -1 weight as indicated in Figs. 1 and 2. To investigate the effect of more sinusoidal transmission functions, we consider the transmitter and receiver geometries shown in Figs. 1 and 2, but with a perfectly sinusoidal transmission function characterized by the filter wavenumber $K_t = 2\pi/\Lambda_f$, where Λ_f is the filter wavelength. We still assume the transmitter and receiver apertures to be rectangular with the same vertical dimension but with a constant length of 40 cm. The transmission functions of the transmitter and receiver filters then have the same form:

$$F_{t,r}\left(\frac{a}{L_t}, \frac{b}{H_t}\right) = \frac{1}{2} \, sinc\left(\frac{b}{2}\right) \left\{ sinc\left[\frac{1}{2}(a + 2\pi N_{t,r})\right] - sinc\left[\frac{1}{2}(a - 2\pi N_{t,r})\right] \right\} . \quad (10)$$

10

Here we have assumed $\gamma = \gamma' = 1$. The corresponding path weighting functions shown in Fig. 4 were found by substituting (10) into (8) for the different cases listed in Table 1. The expected sidelobe suppression due to a more ideal sinusoidal modulation is evident. The locations of the peaks again agree very closely with their expected position. The path resolution Δ agrees mores closely with the predicted result than the previous case because of the closer agreement of this spatial filter model to that used to calculate Δ.
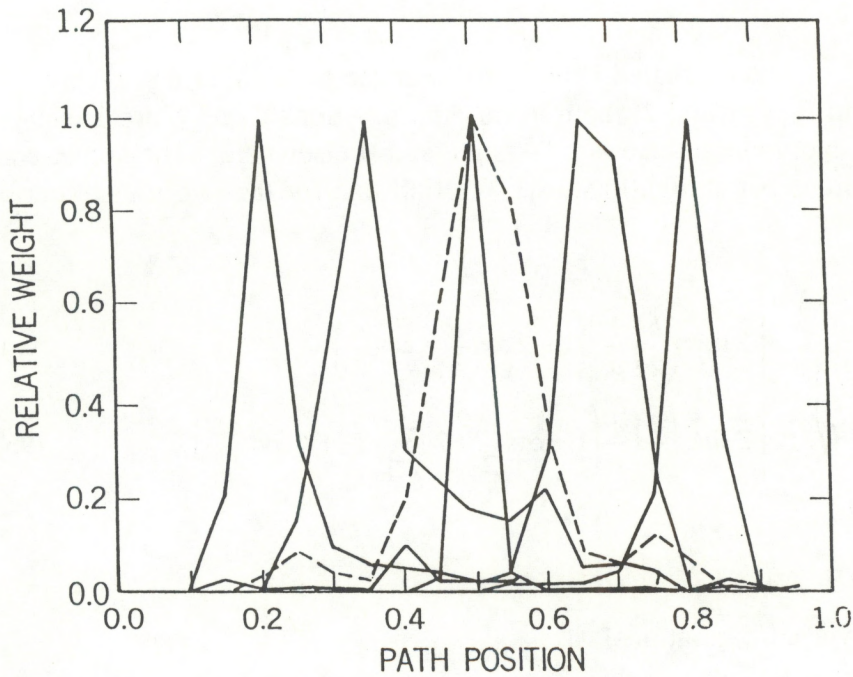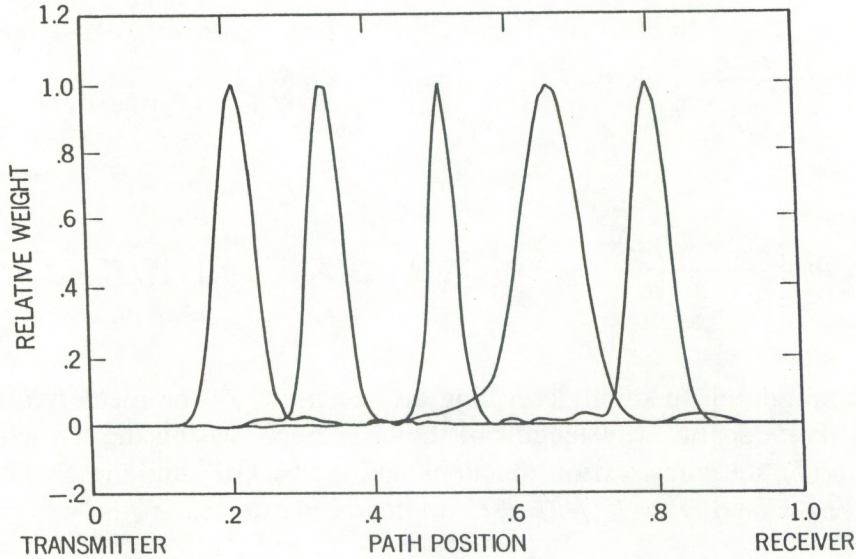

Figure 4. The relative path weight, computed from $W(u)$ defined by (8) and the transmission function defined by (10), is shown plotted as a function of the normalized path position $u = z/L$ for the sinusoidal analogue of the transmitter and receiver configuration shown in Figs. 1 and 2. A path length $L = 1$ km and wavelength $\lambda = 0.93 \mu$ were used in the calculations.

The wind speed is inferred from the frequency of the spatially filtered signal, which depends on the sampled spatial wavenumber K_0, or, equivalently, on the sampled spatial wavelength $\Lambda_0 = 2\pi/K_0$. The expected values of Λ_0 based on (1a) are shown in Table 1. The exact wavenumber response of a particular transmitter-receiver pair combination can be calculated by recasting (6b) in a slightly different form. By assuming that the velocity $V_x(u)$ is constant across the resolution cell of the system, we can replace it in (6b) by $V_x(u_0)$ and write

$$\bar{\omega} = |V_x(u_0)| \bar{K}_x, \qquad (11a)$$

11

where

$$\tilde{K}_x \equiv \int_0^\infty dK_x K_x G(K_x) \tag{11b}$$

is a mean wavenumber and

$$G(K_x) = \frac{16\pi k^2 L}{\int_0^1 du\, W'(u)} \int_0^1 du\, \sin(K_x \rho_x u) \int_0^\infty dK_y\, \Phi_n(K_x, K_y, u)$$

$$\times \sin^2\left[\frac{(K_x^2 + K_y^2)\, Lu(1-u)}{2k}\right] |F_t[K_x(1-u), K_y(1-u)]|^2\ |F_r(K_x u, K_y u)|^2 \tag{11c}$$

is the wavenumber weighting function describing the sensitivity of the mean frequency measurement to different spatial wavelengths of the turbulence. Using the refractive index spectrum defined in (7), the transmission functions defined by (10), and the change of variables $x' = K_x\sqrt{L/2k}$ and $y' = K_y\sqrt{L/2k}$, (11c) can be written as

$$G(x') = \frac{0.66\, k^{2/3} L^{7/3} C_n^2}{\int_0^1 du\, W'(u)} \int_0^1 du\, \sin(a'x'u) \int_0^\infty dy'\, \frac{1}{(x'^2 + y'^2)^{11/6}}$$

$$\times \sin^2 |[(x'^2 + y'^2)\, u(1-u)]| \left|F_t\left[\frac{x'}{\sqrt{L/2k}}(1-u), \frac{y'}{\sqrt{L/2k}}(1-u)\right]\right|^2 \left|F_r\left(\frac{x'}{\sqrt{L/2k}}u, \frac{y'}{\sqrt{L/2k}}u\right)\right|^2 , \tag{12a}$$

where

$$\left|F_{t,r}\left(\frac{x'}{\sqrt{L/2k}}, \frac{y'}{\sqrt{L/2k}}\right)\right|^2 = \frac{1}{4} sinc^2\left(\frac{y'}{2\epsilon}\right)\left\{ sinc\left[\frac{1}{2}\left(\frac{x'}{\delta} + 2\pi N_{t,r}\right)\right]\right.$$

$$\left. - sinc\left[\frac{1}{2}\left(\frac{x'}{\delta} - 2\pi N_{t,r}\right)\right]\right\}^2 , \tag{12b}$$

12

$a' = \rho_x / \sqrt{L/2k}$, $\epsilon = \sqrt{L/2k}/H$, $H = H_t = H_r$, $\delta = \sqrt{L/2k}/L'$, $L' = L_t = L_r$ and
$N_{t,r} = L'/\Lambda_{t,r}$.

Figures 5a and 5b show $G(x')$ plotted on a relative scale as a function of the normalized wavenumber $x' = K_x \sqrt{L/2k}$ for the transmitter-receiver pair combinations described in lines 1 and 3 of Table 1, respectively. We have again used $L = 1$ km and $\lambda = 0.93\ \mu$, which gives $\sqrt{L/2K} = 0.86$ cm. The peak and mean wavenumbers are essentially the same in each of the figures. The mean normalized wavenumber $\tilde{x}'$ in Fig. 5a is 1.36, which corresponds to a mean wavenumber $\tilde{K}_x = \tilde{x}'/\sqrt{L/2k} = 1.58\ cm^{-1}$ and a mean spatial wavelength $\Lambda_x = \tilde{K}_x/(2\pi) = 3.97\ cm$. This agrees almost exactly with the predicted value of 4.00 for Λ_0 in line 1 of Table 1. The mean normalized wavenumber $\tilde{x}'$ in Fig. 5b is 2.16, which corresponds to a mean wavenumber $\tilde{K}_x = 2.51\ cm^{-1}$ and a mean spatial wavelength $\Lambda_x = 2.50\ cm$. This is exactly the predicted result for Λ_0 in line 4 of Table 1. The other spatial filter combinations produce a similar agreement. Equation (1b) therefore accurately predicts the spatial wavenumber sampled by the system.
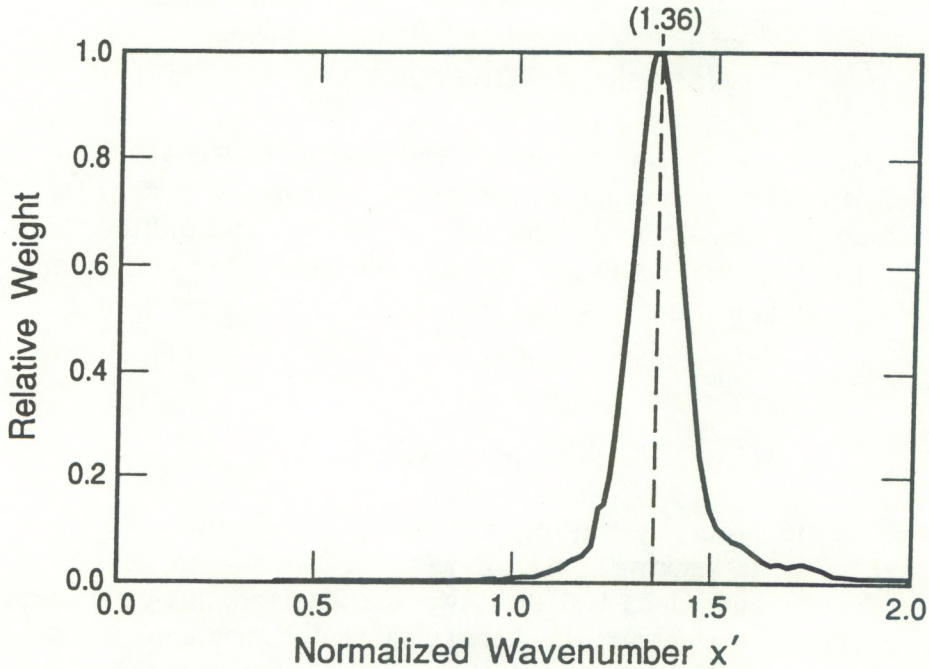
Figure 5a. The relative wavenumber weight computed from $G(x')$ defined in (12a) plotted as a function of the normalized wavenumber $x' = K_x \sqrt{L/2k}$ for the transmitter-receiver pair combination described in line 1 of Table 1. A pathlength $L = 1$ km and wavelength $\lambda = 0.93\ \mu$m were used in the calculations. The vertical dashed line is the location of the mean wavenumber $\tilde{x}'$.
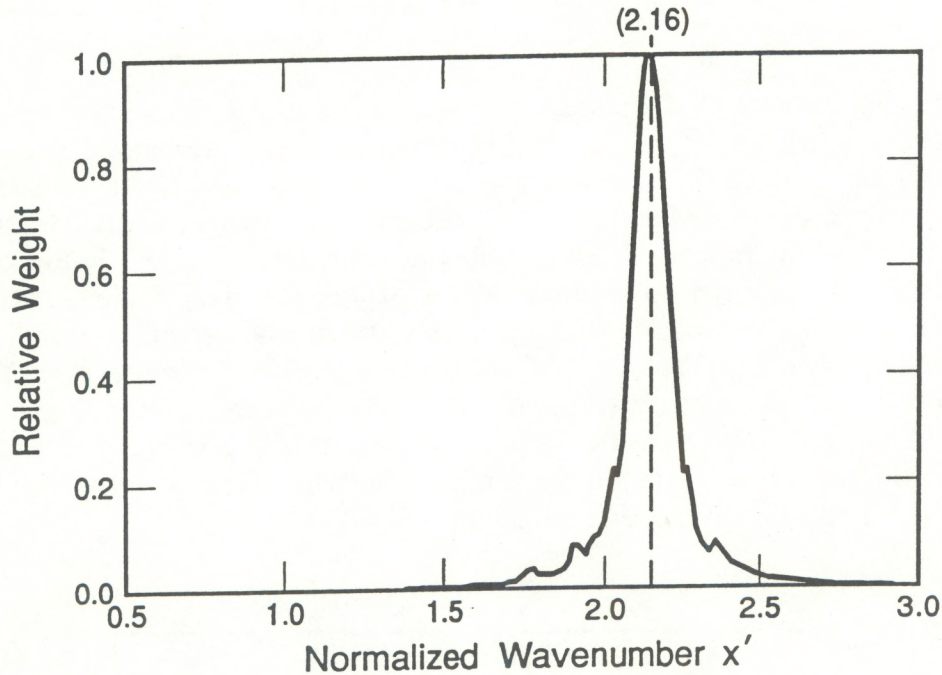
Figure 5b. The relative wavenumber weight computed from $G(x')$ defined in (12a) plotted as a function of the normalized wavenumber $x' = K_x \sqrt{L/2k}$ for the transmitter-receiver pair combination described in line 4 of Table 1. A pathlength $L = 1$ km and wavelength $\lambda = 0.93 \ \mu$m were used in the calculations. The vertical dashed line is the location of the mean wavenumber $\tilde{x}'$.

3. PERFORMANCE

Initial testing of the profiler system began in April 1987, after which a number of design changes were made that improved performance. When these were completed, the tests described here were carried out. Units 1, 2, and 3 were tested during the period September through November 1987, after which unit 1 was retained by WPL and units 2 and 3 were delivered to the research sponsor. A fourth unit was completed and tested with unit 1 during April through June 1989. Generally, the tests were performed to determine the wind speed measurement accuracy, the wind profiling capability and how well it compared with theory, and the range of refractive-index turbulence (C_n^2) over which the system would operate.

Testing was done on a 500-m north-south path, 1.5 m above the surface of Table Mountain, a flat-topped mesa 12 km north of Boulder, Colorado. The system wind measurements were compared to the readings of five propeller anemometers (Gill Model No. 27106) mounted horizontally at right angles to the optical path. A low wind-speed correction recommended by Gill has been applied to readings less than 1 m s^{-1}. The anemometers were

14

located at the five positions along the optical path where the maximum system response to wind was expected, i.e., 0.20, 0.33, 0.50, 0.67, and 0.80 of the distance from the transmitter to the receiver. A 4.4-cm-diameter incoherent optical scintillometer, operating over a nearby 250-m path, measured the refractive-index structure parameter (C_n^2). Some long-term average comparisons of profiler and anemometer measurements are given in Table 2.

Table 2. Some comparisons of long-term average crosswind measurements from anemometers and the optical systems. The averages of the five optical readings and all of the anemometer readings are compared. The number of anemometers used is indicated in parentheses.

Date	Serial Number	Time Period	Profiler Ave., m s^{-1}	Anemometer Ave., m s^{-1}	Ratio Prof./Ane.
25 Oct 87	2	10 min	4.93+0.23	5.07+0.39 (5)	0.97
29 Oct 87	3	20 h	0.8 +0.07	0.92+0.13 (5)	0.87
	2	20 h	0.8 +0.07	0.92+0.13 (5)	0.87
	3	5 min	2.8 +0.19	2.8 +0.28 (5)	1.0
	2	5 min	2.76+0.15	2.8 +0.28 (5)	0.99
3 Nov 87	1	5 min	2.84+0.30	2.82+0.46 (10)	1.01
	1	5 min	4.3 +0.34	4.21+0.62 (10)	1.02
	1	20 h	0.88+0.04	0.93+0.15 (10)	0.95
4 Nov 87	3	100 s	1.56+0.09	1.32+0.08 (5)	1.18
	2	100 s	1.52+0.13	1.32+0.08 (5)	1.18
15 Jan 88	1	55 min	10.62+0.94	10.38 (1)	1.02

The profiler average is the average of all five profiler crosswind readings, with the standard deviation of the five readings. The number of anemometers averaged is shown in parentheses. The profiler calibration is derived from

$$V_0 = V(z_0) = k f_0 \Lambda_0 \qquad (13)$$

where V_0 is the crosswind at the path position z_o, f is the mean frequency measured, Λ_0 is the spatial wavelength of the filter at each location, and k=0.83 is a correction factor. The analysis technique determines the mean frequency by measuring the time delay to the centroid of the minus and plus areas of the covariance function. This necessitates a correction factor to account for the effect of the decay of the scintillation pattern, which causes the mean measured frequency to be slightly higher than if no decay occurred. It is not constant. In principle, it could be calculated, but in this instrument an average value determined experimentally is used. Figure 6 shows a typical measured covariance function.
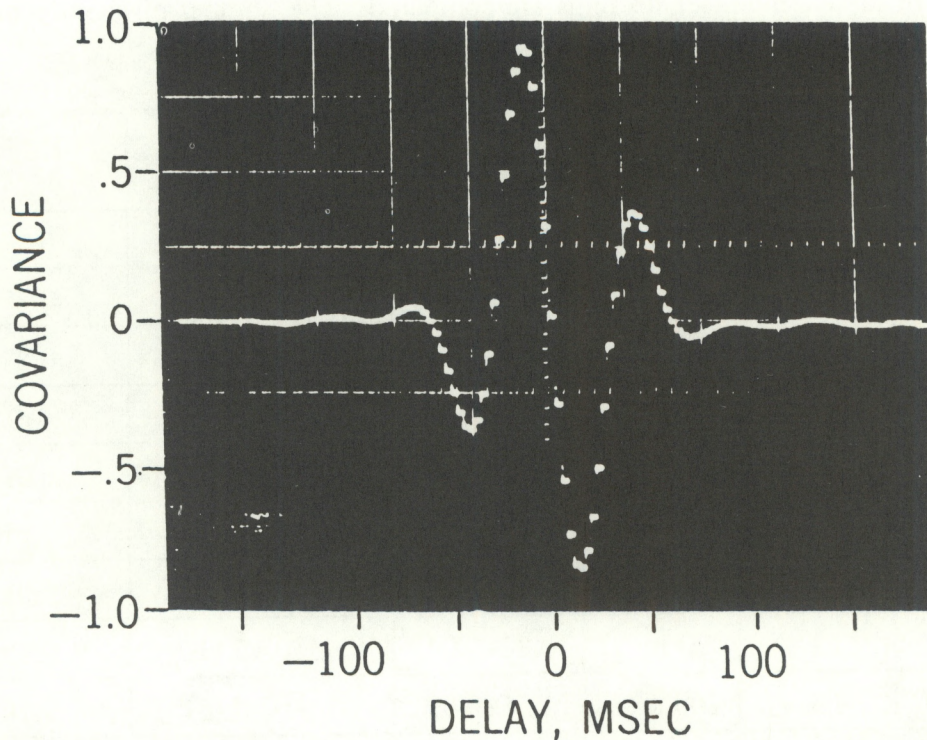
Figure 6. A measured covariance function from the midpath position (2.5-cm wavelength). Wind speed is 0.8 m s^{-1}.

The average of all anemometers used, together with the standard deviation of the average, is also listed in Table 2, and the number averaged is indicated in parentheses. When five anemometers were used, they were located at the peak of the five crosswind profiler responses. The 15 January 1988 high wind data were compared with data from a single Aerovane anemometer during a period when the wind direction was directly across the optical path. Typical comparisons of propeller and crosswind profiler wind measurements for each individual path position are shown in Figs. 7, 8, 9, 10, and 11. Each point is a 5-min average.
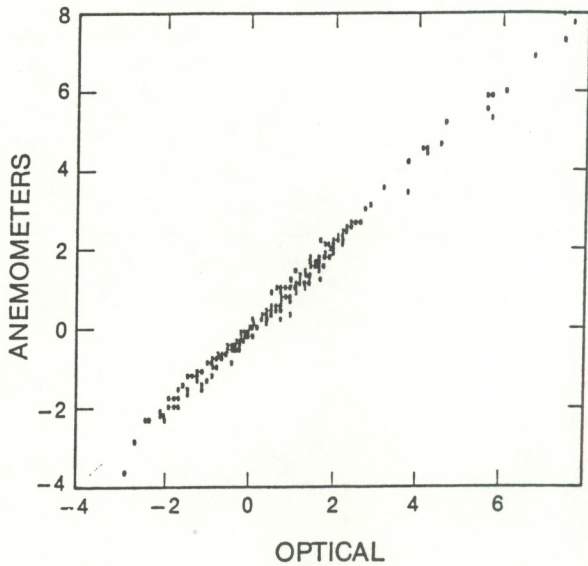
Figure 7. Comparison of optical and propeller anemometer crosswind measurements one-fifth of the path distance from the transmitter. Each point is a 5-min average.
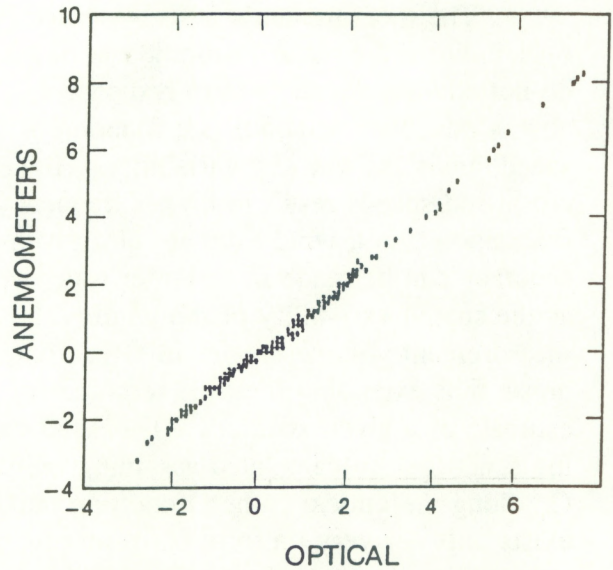
Figure 8. Comparison of optical and propeller anemometer crosswind measurements one-third of the path distance from the transmitter. Each point is a 5-min average.
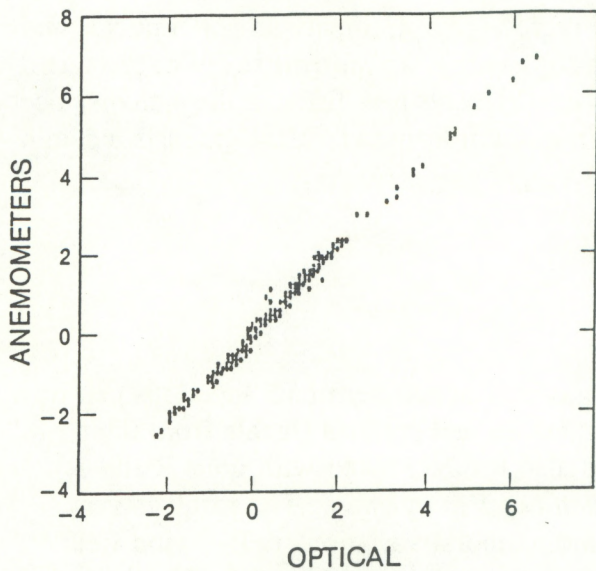
Figure 9. Comparison of optical and propeller anemometer crosswind measurements one-half of the path distance from the transmitter. Each point is a 5-min average.
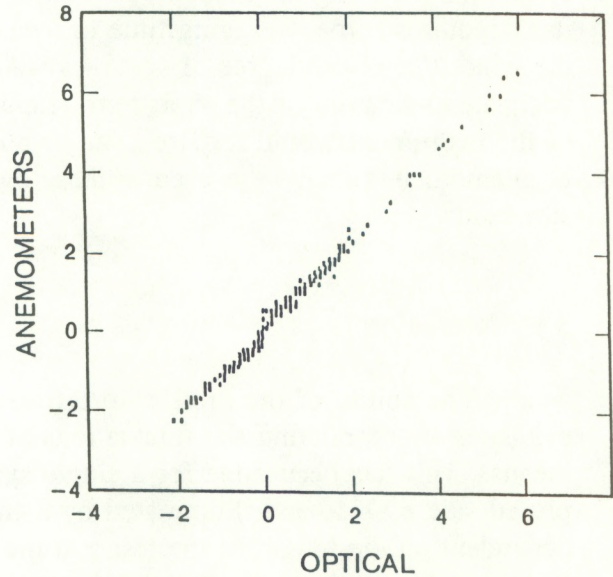
Figure 10. Comparison of optical and propeller anemometer crosswind measurements two-thirds of the path distance from the transmitter. Each point is a 5-min average.

The measurements in Table 2 and Figs. 6-11 indicate the mean calibration accuracy but do not address the short-term response to variable winds. This response is a function of wind speed, and wind and C_n^2 variability. Higher crosswind speeds result in higher frequency fluctuations, so a wind estimate of a given accuracy can be made in a shorter time, whereas the spatial variability of the wind within the measurement volume creates in effect extra noise, thus extending the time required for an estimate of a given accuracy. The wind weighting functions are calculated assuming uniform C_n^2 along the optical path, a condition that exists only for very uniform paths and for long-term averages. Instantaneously, the effective weighting function is very different from the calculated one. The difference between the instantaneous and long-term average weighting functions diminishes the accuracy of the short-term estimate. In addition to the atmospheric conditions affecting the response, the instrument itself requires some averaging time to measure the wind to a given degree of accuracy. An adequate evaluation of the short-term response of the instrument would require a larger number of anemometers than were used in these measurements.

Figure 11. Comparison of optical and propeller anemometer crosswind measurements four-fifths of the path distance from the transmitter. Each point is a 5-min average.

3.1 Correlation

The ability of the profiler to differentiate crosswinds at different path locations can be evaluated by correlating the fluctuations of the anemometer and profiler signals from their means. This has been done for a single system, and also for data taken with units 2 and 3 placed side by side and illuminated by a single transmitter 500 m away. The result is very dependent on the length of the test and the spatial and temporal variations in the wind field. It does indicate where the peak of the crosswind response occurs along the optical path, however. Additional information is available about the irregularity of the wind and the precision of the measurement by calculating a correlation matrix of all combinations of anemometer and profiler measurements. A number of these correlation matrices are listed in Tables 3 through 10. In all tables, the path position from transmitter to receiver increases from top to bottom and from left to right in the listings. For Tables 3, 4, 5, and 10, the five anemometers were located at 0.2, 0.33, 0.5, 0.67, and 0.8 of the distance from the transmitter

18

to the receiver, i.e., the locations where the optical wind measurements were expected to peak. In Tables 6, 7, 8, and 9, five more anemometers were added between the original five, so that the 10 were located 0.2, 0.25, 0.33, 0.42, 0.5, 0.58, 0.67, 0.75, 0.8, and 0.92 of the distance from the transmitter to the receiver. All the anemometers were oriented to measure the horizontal component of the wind at right angles to the optical path.

Table 3 was calculated from 249 1-s samples when the crosswind was about 1.5 m s^{-1}. Except for correlations involving the defective 0.67 position of profiler serial 3, both serials 2 and 3 show maximum correlation with the appropriate anemometers. One of the main reasons the correlations are as low as 0.3 to 0.6 is that the anemometer is making nearly a point measurement as compared to the line average represented by the weighting function of the profiler for that position. A smaller contributing factor is caused by the anemometers being slightly displaced from the optical line of sight so there is a slight time delay as the wind flows across the anemometers to the optical path. A better idea of the precision of the measurement is obtained from the correlation (0.9 or greater) of the positions of profiler units 2 and 3. The time delay factor remains since the optical paths of these units diverge from a single transmitter to the receivers, but both systems should be measuring nearly the same line average for their positions. The anemometer measurements indicate that the wind fluctuations from these point measurements are essentially uncorrelated. There is some correlation between the different path positions along each profiler path. One would expect this since the line averaging taking place in the optical instruments restricts the wind measurement to larger spatial sizes. Table 4 is another set of data using 100 1-s samples and taken under very similar wind conditions, with very similar results.

Table 5 shows data obtained from 200 10-s average samples taken from a larger sample of the same data set where the average crosswind was 1.5 m s^{-1}. As expected, all the correlations are higher. Table 6 was calculated from 249 10-s average samples on a different date when the average crosswind was 2.6 m s^{-1}. In this case, one optical profiler is compared with 10 anemometers along the path. The slightly higher wind speed probably reduced the spatial irregularity of the wind, resulting in even higher correlations for all combinations. A larger sample of data from this same set was used to calculate correlations from 24 100-s average samples in Table 7. Again, the largest profiler-anemometer correlations occur at the proper locations along the path.

Table 8 contains information from 249 5-min average samples during average crosswinds of 0.9 m s^{-1}. Table 9 is from 249 5-min average samples during average crosswinds of 4.3 m s^{-1}. For these data, 10 anemometers were compared with the serial 1 profiler. Finally, Table 10 is from 249 5-min average samples, and compares serial 2 and 3 profilers with five anemometers. The data in Tables 8, 9, .and 10 are of little use in determining the weighting, since the 5-min averaged wind data are very well correlated over the whole optical path. Nevertheless, the highest correlation occurs with the anemometer at the predicted location, and between the outputs of the serial 2 and 3 profilers.

Table 3. Correlation matrix of wind measurements from five anemometers located at 0.2, 0.33, 0.5, 0.67, and 0.8 of the path distance from the transmitter, and the corresponding wind measurements from crosswind profilers serial 2 and serial 3. Path position increases from top to bottom and left to right. The correlations were calculated from 249 1-s samples.

	Serial 3					Serial 2					Anemometers				
Serial 3	0.678														
	0.342	0.353													
	0.066	0.179	0.301												
	0.069	0.242	0.301	0.399											
Serial 2	0.956	0.649	0.344	0.061	0.084										
	0.692	0.952	0.322	0.162	0.175	0.660									
	0.375	0.407	0.950	0.277	0.325	0.381	0.377								
	0.069	0.255	0.467	0.365	0.580	0.073	0.228	0.473							
	-.003	0.166	0.334	0.413	0.900	0.006	0.112	0.336	0.579						
Anemometers	0.584	0.414	0.316	-.062	0.073	0.629	0.411	0.351	0.146	0.022					
	0.192	0.464	0.064	0.167	0.008	0.155	0.487	0.069	-.029	-.053	-.004				
	-.029	-.015	0.515	0.141	0.038	-.007	-.035	0.546	0.207	0.068	0.207	-.057			
	-.293	-.202	0.161	-.034	0.009	-.240	-.194	0.134	0.296	0.047	0.001	-.079	0.212		
	-.168	-.113	-.153	-.092	0.276	-.141	-.152	-.169	0.000	0.288	-.064	-.158	-.065	0.084	

Table 4. Correlation matrix of wind measurements from five anemometers located at 0.2, 0.33, 0.5, 0.67, and 0.8 of the path distance from the transmitter, and the corresponding wind measurements from crosswind profilers serial 2 and serial 3. Path position increases from top to bottom and left to right. The correlations were calculated from 100 1-s samples.

	Serial 3					Serial 2					Anemometers				
Serial 3	0.820														
	0.639	0.656													
	0.381	0.348	0.223												
	-.041	0.200	0.164	0.267											
Serial 2	0.949	0.786	0.637	0.342	-.015										
	0.854	0.970	0.679	0.391	0.140	0.813									
	0.637	0.708	0.939	0.213	0.190	0.640	0.725								
	0.301	0.427	0.441	0.404	0.644	0.338	0.409	0.482							
	-.146	0.082	0.114	0.275	0.904	-.126	0.029	0.116	0.567						
Anemometers	0.652	0.425	0.403	0.089	-.139	0.695	0.448	0.436	0.171	-.233					
	0.582	0.733	0.382	0.467	0.230	0.530	0.762	0.411	0.281	0.197	0.216				
	0.192	0.142	0.401	0.059	-.218	0.236	0.188	0.428	0.031	-.215	0.240	0.061			
	-.215	-.146	0.105	-.281	-.021	-.135	-.168	0.099	0.104	0.011	0.029	-.237	0.220		
	-.383	-.345	-.068	-.356	0.184	-.315	-.392	-.097	-.106	0.253	-.218	-.346	-.043	0.143	

Table 5. Correlation matrix of wind measurements from five anemometers located at 0.2, 0.33, 0.5, 0.67, and 0.8 of the path distance from the transmitter, and the corresponding wind measurements from crosswind profilers serial 2 and serial 3. Path position increases from top to bottom and left to right. The correlations were calculated from 249 10-s averages.

	Serial 3					Serial 2					Anemometers			
Serial 3	0.604													
	0.380	0.530												
	0.344	0.527	0.710											
	0.321	0.512	0.650	0.765										
Serial 2	0.984	0.627	0.414	0.362	0.367									
	0.595	0.987	0.541	0.556	0.545	0.622								
	0.393	0.559	0.991	0.705	0.654	0.429	0.569							
	0.445	0.629	0.733	0.885	0.791	0.469	0.656	0.733						
	0.298	0.487	0.664	0.813	0.955	0.325.	0.517	0.663	0.811					
Anemometers	0.768	0.399	0.372	0.304	0.255	0.780	0.407	0.378	0.378	0.246				
	0.408	0.787	0.467	0.515	0.447	0.431	0.798	0.487	0.566	0.438	0.321			
	0.224	0.364	0.848	0.606	0.534	0.253	0.378	0.854	0.584	0.561	0.317	0.395		
	0.320	0.484	0.597	0.714	0.675	0.355	0.509	0.602	0.827	0.658	0.345	0.498	0.528	
	0.102	0.272	0.413	0.579	0.779	0.125	0.305	0.409	0.541	0.791	0.112	0.253	0.397	0.474

Serial 3   Serial 2   Anemometers

Table 6. Correlation matrix of wind measurements from 10 anemometers located at 0.2, 0.25, 0.33, 0.42, 0.5, 0.58, 0.67, 0.75, 0.8, and 0.92 of the path distance from the transmitter, and the five wind measurements from crosswind profiler serial 1. The correlations are from 249 10-s samples.

	Serial 1					Anemometers								
Serial 1	0.939													
	0.908	0.909												
	0.860	0.867	0.921											
	0.839	0.837	0.902	0.953										
Anemometers	0.935	0.877	0.843	0.791	0.768									
	0.875	0.867	0.827	0.786	0.778	0.835								
	0.852	0.935	0.839	0.793	0.765	0.822	0.811							
	0.860	0.878	0.848	0.823	0.792	0.825	0.838	0.827						
	0.820	0.832	0.926	0.849	0.844	0.768	0.785	0.772	0.800					
	0.800	0.798	0.843	0.859	0.853	0.752	0.770	0.744	0.748	0.793				
	0.772	0.773	0.787	0.883	0.834	0.729	0.716	0.724	0.724	0.735	0.766			
	0.769	0.758	0.801	0.876	0.894	0.715	0.680	0.695	0.708	0.760	0.756	0.789		
	0.731	0.737	0.778	0.832	0.901	0.679	0.687	0.683	0.703	0.741	0.705	0.726	0.805	
	0.748	0.769	0.805	0.818	0.842	0.704	0.746	0.714	0.717	0.759	0.791	0.741	0.765	0.768

Serial 1   Anemometers

Table 7. Correlation matrix of wind measurements from 10 anemometers located at 0.2, 0.25, 0.33, 0.42, 0.5, 0.58, 0.67, 0.75, 0.8, and 0.92 of the path distance from the transmitter, and the five wind measurements from crosswind profiler 1. The correlations are from 24 100-s samples.

```
Serial 1
0.990
0.952  0.961
0.903  0.920  0.961
0.894  0.913  0.958  0.979

Anemometers                              | Serial 1 / Anemometers
0.984  0.974  0.937  0.884  0.874
0.980  0.977  0.929  0.888  0.883 | 0.980
0.967  0.985  0.941  0.897  0.893 | 0.970  0.972
0.971  0.979  0.954  0.915  0.899 | 0.977  0.974  0.981
0.920  0.936  0.985  0.954  0.967 | 0.910  0.915  0.926  0.938
0.920  0.938  0.950  0.956  0.952 | 0.909  0.916  0.925  0.924  0.949
0.875  0.890  0.907  0.969  0.943 | 0.864  0.883  0.876  0.907  0.916  0.940
0.862  0.883  0.919  0.970  0.979 | 0.845  0.853  0.864  0.878  0.929  0.943  0.952
0.879  0.892  0.938  0.966  0.985 | 0.870  0.873  0.873  0.891  0.948  0.922  0.939  0.975
0.873  0.901  0.912  0.929  0.952 | 0.866  0.889  0.887  0.900  0.932  0.943  0.927  0.959  0.947
         Serial 1                                Anemometers
```

Table 8. Correlation matrix of wind measurements from 10 anemometers located at 0.2, 0.25, 0.33, 0.42, 0.5, 0.58, 0.67, 0.75, 0.8, and 0.92 of the path distance from the transmitter and the five wind measurements from crosswind profiler serial 1. The correlations are from 249 5-min samples.

```
Serial 1
0.993
0.979  0.990
0.977  0.984  0.989
0.970  0.980  0.990  0.990

Anemometers                              | Serial 1 / Anemometers
0.989  0.986  0.974  0.980  0.966
0.919  0.922  0.918  0.887  0.907 | 0.891
0.985  0.993  0.981  0.985  0.973 | 0.993  0.897
0.977  0.987  0.983  0.986  0.974 | 0.987  0.885  0.993
0.968  0.979  0.989  0.988  0.982 | 0.976  0.891  0.982  0.990
0.963  0.974  0.984  0.989  0.987 | 0.970  0.881  0.977  0.983  0.991
0.968  0.979  0.986  0.990  0.992 | 0.971  0.895  0.979  0.981  0.985  0.991
0.967  0.975  0.984  0.986  0.994 | 0.966  0.893  0.972  0.974  0.978  0.986  0.994
0.964  0.972  0.981  0.984  0.994 | 0.963  0.886  0.969  0.970  0.975  0.983  0.990  0.995
0.958  0.964  0.972  0.976  0.987 | 0.956  0.876  0.960  0.960  0.964  0.975  0.981  0.987  0.993
         Serial 1                                Anemometers
```

Table 9. Correlation matrix of wind measurements from 10 anemometers located at 0.2, 0.25, 0.33, 0.42, 0.5, 0.58, 0.67, 0.75, 0.8, and 0.92 of the path distance from the transmitter and the five wind measurements from crosswind profiler serial 1. The correlations are from 249 10-min samples.

```
Serial 1
0.995
0.988  0.993
0.983  0.987  0.990
0.984  0.988  0.994  0.994

Anemometers
0.991  0.989  0.983  0.980  0.980
0.964  0.966  0.963  0.948  0.956 | 0.954
0.990  0.994  0.989  0.986  0.986 | 0.995  0.959
0.986  0.990  0.990  0.988  0.988 | 0.991  0.954  0.995
0.981  0.985  0.990  0.987  0.989 | 0.986  0.947  0.991  0.995
0.977  0.981  0.987  0.988  0.990 | 0.982  0.944  0.987  0.993  0.996
0.978  0.982  0.987  0.988  0.991 | 0.981  0.946  0.986  0.989  0.993  0.995
0.978  0.982  0.987  0.987  0.993 | 0.979  0.950  0.985  0.987  0.990  0.992  0.994
0.978  0.982  0.986  0.987  0.993 | 0.977  0.948  0.984  0.984  0.987  0.988  0.992  0.996
0.972  0.976  0.980  0.983  0.989 | 0.972  0.944  0.979  0.980  0.982  0.985  0.986  0.989  0.992
        Serial 1                                    Anemometers
```

Table 10. Correlation matrix of wind measurements from five anemometers located at 0.2, 0.33, 0.5, 0.67, and 0.8 of the path distance from the transmitter, and the corresponding wind measurements from crosswind profilers serial 2 and serial 3. Path position increases from top to bottom and left to right. The correlations 15 were calculated from 249 5-min averages.

```
Serial 3
0.98
0.96  0.99
0.97  0.99  0.99
0.96  0.98  0.99  0.99

Serial 2
0.99  0.99  0.97  0.97  0.96
0.97  0.99  0.98  0.98  0.97 | 0.98
0.97  0.99  1.00  0.99  0.99 | 0.97  0.98
0.97  0.99  0.99  1.00  0.99 | 0.97  0.98  0.99
0.96  0.98  0.98  0.99  1.00 | 0.96  0.97  0.99  0.99

Anemometers
0.97  0.98  0.97  0.97  0.97 | 0.98  0.98  0.97  0.97  0.96
0.97  0.99  0.98  0.98  0.97 | 0.97  0.98  0.98  0.98  0.97 | 0.99
0.95  0.98  0.99  0.99  0.98 | 0.96  0.97  0.99  0.99  0.98 | 0.97  0.98
0.95  0.97  0.98  0.99  0.99 | 0.95  0.97  0.99  0.99  0.98 | 0.96  0.97  0.99
0.95  0.97  0.98  0.99  0.99 | 0.95  0.96  0.98  0.99  0.99 | 0.97  0.97  0.98  0.99
      Serial 3                       Serial 2                      Anemometers
```

23

3.2 Weighting function

Another way to evaluate how well the profiler distinguishes crosswinds at different path locations, that is not so dependent upon the time average, is to solve a series of linear equations of data taken sequentially, of the form

$$100\,V_0 = K_1 V_1 + K_2 V_2 + K_3 V_3 + K_4 V_4 + K_5 V_5 , \tag{14}$$

where V_o is the profiler wind reading for a particular path position, V_1 through V_5 are the anemometer readings at the peak of the five crosswind profiler responses, and K_1 through K_5 are the weighting factors. The ideal comparison wind measurement would have a weighting function the same as the crosswind profiler for each path location. The anemometers, however, are essentially a point measurement and must be averaged over some time period to correspond better to the space average of the crosswind profiler. Since the correspondence is not exact, it is better to use more than the minimum five equations required (49 were used for the following data) and solve for the least-squares best fit weights.

Tables 11 and 12 show the weighting functions obtained on a 500-m path for units 2 and 3. We used 196 samples, each sample consisting of an average of 10 of the original 1-s samples. Note that the 0.67 position for unit 3 was not operating properly. Some information about the precision of the measurement can be obtained by using the same technique to compare serials 2 and 3. This was done by illuminating the two receiving units, placed side by side, with one transmitter 500 m away. Again, 196 samples were used, each sample consisting of an average of 10 of the original 1-s samples. The result is shown in Table 13.

Table 11. Wind weighting matrix, profiler unit 3 versus anemometers.

Anemometers

Path Position	0.20	0.33	0.50	0.67	0.80
0.20	28	10	- 1	3	- 4
0.33	2	36	- 2	2	3
0.50	3	6	29	- 4	- 4
0.67	5	11	4	- 2	- 1
0.80	3	0	2	3	16

Profiler Serial 3

Table 12. Wind weighting matrix, profiler unit 2 versus anemometers.

Anemometers

Path Position	0.20	0.33	0.50	0.67	0.80
0.20	28	10	- 3	6	- 8
0.33	5	38	- 3	2	2
0.50	3	6	29	- 2	- 4
0.67	4	8	2	15	0
0.80	2	- 2	0	0	14

Profiler Serial 2

Table 13. Wind weighting matrix, profiler unit 2 versus unit 3.

Unit 3

Path Position	0.20	0.33	0.50	0.67	0.80
0.20	89	2	6	- 2	2
0.33	- 2	88	6	1	- 4
0.50	- 1	- 4	100	- 1	2
0.67	- 9	13	0	58	25
0.80	2	0	3	1	86

Profiler Serial 2

These measurements indicate that the wind measurements are taking place at the expected locations but give little information about the actual shape of the weighting functions. Even with many more anemometers, it would not be possible to measure the weighting functions accurately because the natural wind fluctuation correlation length on the test path is too large. Another approach would be to artificially perturb the atmosphere on a small enough scale to determine the weighting functions. Rather than measure wind, we decided that it would be more practical to measure the response to a large increase in C_n^2, and make the assumption that the weighting function for C_n^2 is very close to that for wind. The wind profiler circuits were altered for this test by removing the AGC and computing an

uncalibrated variance measurement from samples taken once per second of each of the five decoded scintillation signals coming from the five path positions. The tests were conducted around the variance minimum occurring just after sunrise. We positioned a kerosene space heater to blow hot air sequentially at 24 positions along the 500-m path. The variance of the signals from the five filters was recorded for all 24 heater positions.

Figures 12 through 16 show the experimental results. The peak responses are close to the locations predicted in Fig. 4. The overall weighting function for the 0.80 position is quite good. The 0.20 position is also reasonable except that the peaks do not match as closely. The others peak at about the expected location, but have spurious responses near the receiver, something that did not occur in the weighting functions measured by observing natural variations of wind. We do not know the reasons for this. One possibility involves the analysis by which the wind speed is measured. This method mainly observes the dominant frequencies that are in quadrature from the two receiving arrays that are displaced by one-quarter wavelength in space, discriminating very effectively against other signals that are present. The response tends to have a capture effect that ignores signals that do not satisfy these criteria. The variance measurement, however, was made with just one of the receiving arrays and most likely includes signals that the wind analysis disregarded. Another possibility is that the zero mean filters, both transmitter and receiver, are not exactly balanced, so that the response to spatial wavelengths outside the passband is greater than expected. The variance measurement would be affected to a greater extent by this error than the wind measurement. Also the turbulence strength of the kerosene heater was not the same at all locations along the path, somewhat because of slight differences in positioning and mostly because of variable light winds deflecting the blower air stream. This would cause some irregular errors in the measurement but is unlikely to account for high signals near the receiver.
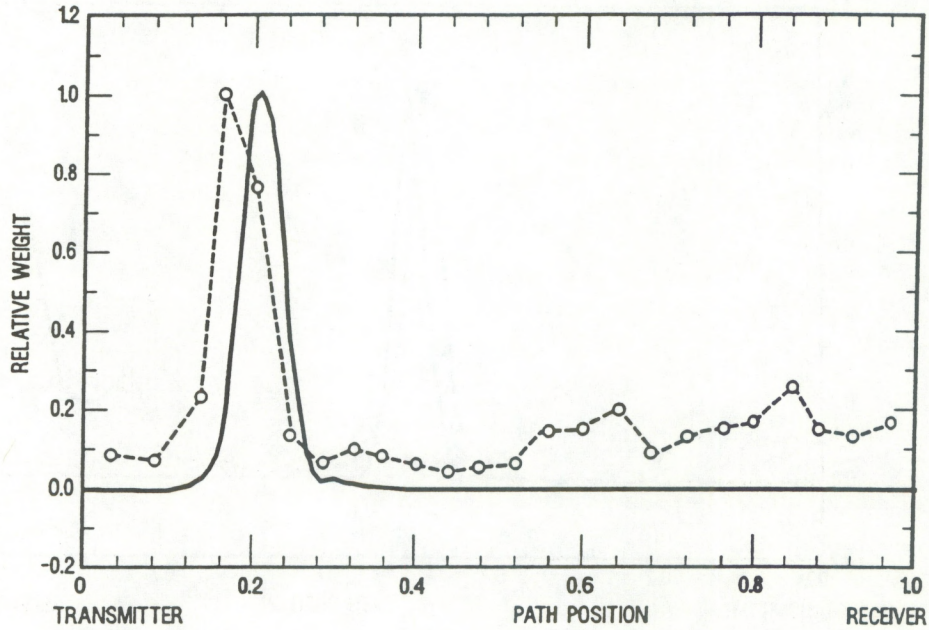
Figure 12. Comparison of the theoretical weighting function for the 0.20 position (solid line) from Fig. 4, with an experimental optical determination (dashed line) obtained by perturbing the turbulence along the path with a kerosene space heater.
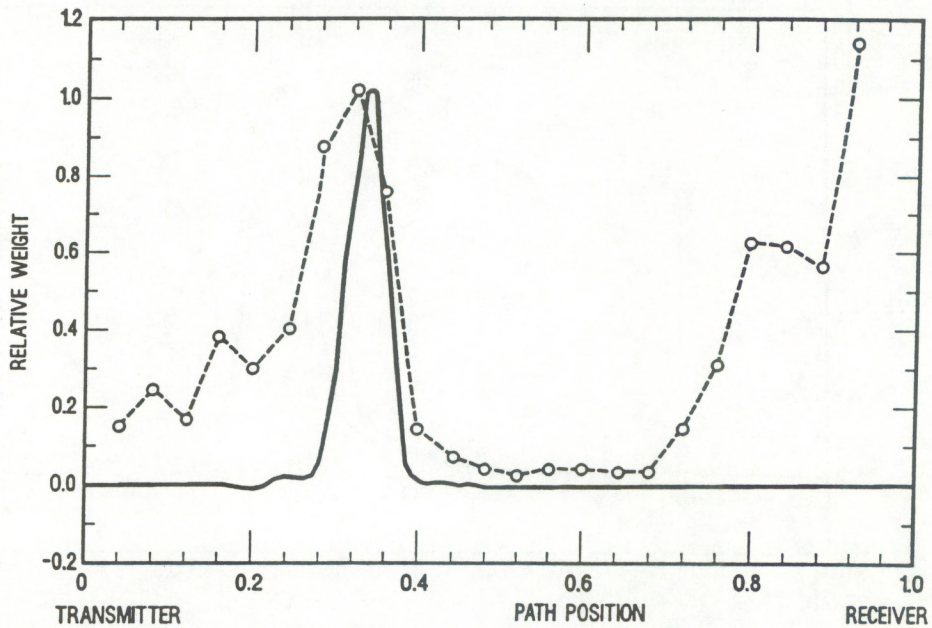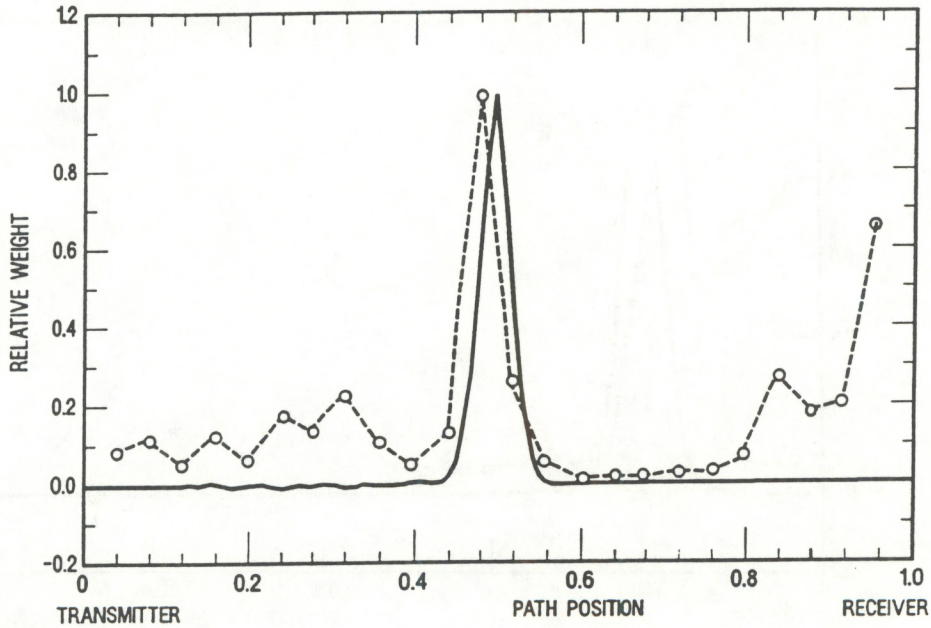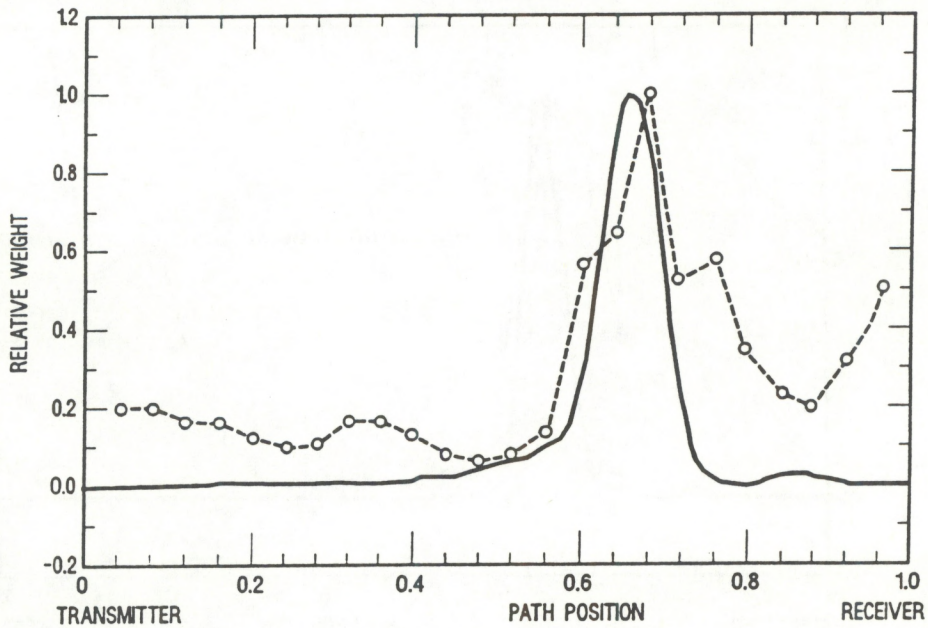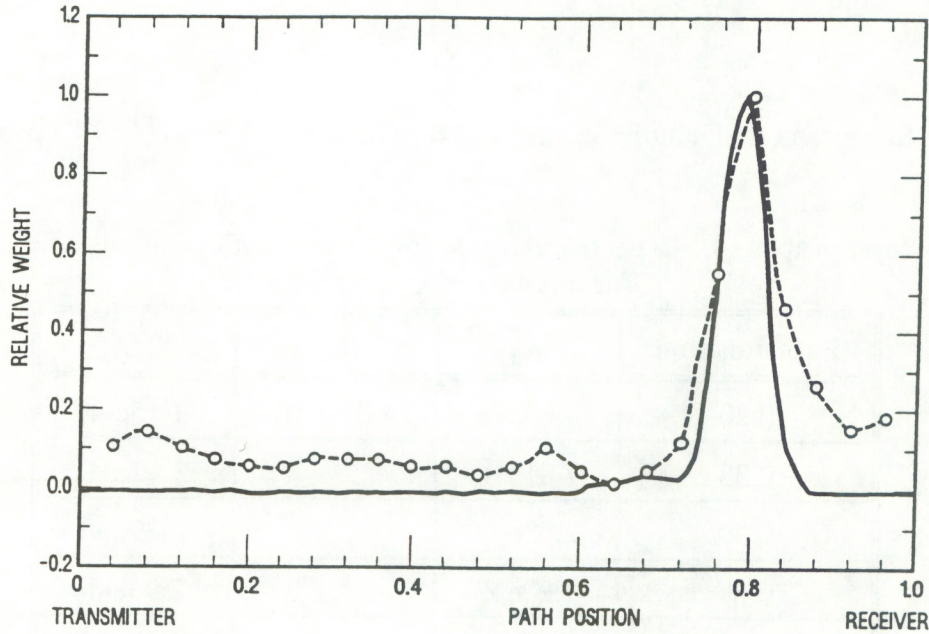

Figure 13. Comparison of the theoretical weighting function for the 0.33 position (solid line) from Fig. 4, with an experimental optical determination (dashed line) obtained by perturbing the turbulence along the path with a kerosene space heater.

27

Figure 14. Comparison of the theoretical weighting function for the 0.50 position (solid line) from Fig. 4, with an experimental optical determination (dashed line) obtained by perturbing the turbulence along the path with a kerosene space heater.

Figure 15. Comparison of the theoretical weighting function for the 0.67 position (solid line) from Fig. 4, with an experimental optical determination (dashed line) obtained by perturbing the turbulence along the path with a kerosene space heater.

28

Figure 16. Comparison of the theoretical weighting function for the 0.80 position (solid line) from Fig. 4, with an experimental optical determination (dashed line) obtained by perturbing the turbulence along the path with a kerosene space heater.

3.3 Turbulence operating range

Relying as the profiler does on refractive-index irregularities as tracers to measure wind, the level of refractive-index turbulence (C_n^2) and its large-scale distribution along the optical path have a major effect on its performance. Unfortunately, C_n^2 in the atmospheric boundary layer can be expected to vary over more than four orders of magnitude, i.e., from less than 10^{-16} to more than 10^{-12} m$^{-2/3}$. This means that the root mean square (RMS) of the intensity fluctuations at the receiver will vary by more than a factor of 100. In general, in an incoherent aperture system, the modulation depth imposed on the signal by refractive-index fluctuations is quite small. For example, the log-amplitude variance σ_χ^2 of an incoherent-aperture scintillometer with an equal-diameter transmitter and receiver is

$$\sigma_{\chi a}^2 = L^3 C_n^2 / (4.474 \, D^{7/3}) = K_a C_n^2 , \tag{15}$$

where D is the aperture diameter and L is the path length. The proportionality constant K_p between C_n^2 and log-amplitude variance $\sigma_{\chi p}^2$ in the profiler,

29

$$\sigma_{\chi P}{}^2 = K_p C_n{}^2, \qquad\qquad (16)$$

is calculated for unsaturated conditions and a 500-m path length in Table 14 (Wang et al., 1991).

Table 14. Expected variance for the five path positions
for unsaturated conditions.

Path Position	K_p	K_a	K_p/K_a
0.20	4.69e+6	4.09e+10	1.15e-4
0.33	7.81e+6		1.91e-4
0.50	2.00e+7		4.89e-4
0.67	1.20e+7		2.93e-4
0.80	4.69e+6		1.15e-4

Thus the expected variance seen by the profiler is about 10^{-4} that of the 15-cm-diameter incoherent-aperture scintillometer. This is not as bleak as it looks, however, partly because of the larger signal from the transmitter and receiver apertures (29 x 40 cm) and mostly because of the covariance analysis technique employed in the wind measurement, which can operate under very poor S/N conditions. The end result is that on a 500-m path, the system can measure winds down to $C_n{}^2$ levels of a few parts in 10^{-16}.

The design is such that some saturation of scintillation occurs, especially for the midpath position, the one that employs 2.5-cm wavelength transmitter and receiver filters. There is minimal change in saturation in the weighting function, and although the variance of the signal decreases significantly, it is still much larger than those signals encountered at low turbulence levels.

The effect of saturation was observed by making slight alterations to the profiler. For this measurement, the automatic gain control was disabled, and the mean square signal fluctuations x^2 were measured simultaneously from the two transmitting and receiving spatial filter sets that peak in the center of the path. The 2.5-cm transmitting filter is on top of the 10-cm filter, and the receiving filters are coincident. The 15-min averages of all three measurements were made over 23 hours. Figure 17 is a log-log plot of the variance of the 10-cm filter versus the $C_n{}^2$ obtained from a separate incoherent-aperture scintillometer, and Fig. 18 is a log-log plot of the variance versus $C_n{}^2$ for the 2.5-cm filter. A 5-point running average has been applied to all the graphs. Although the log-intensity variances are reduced by an order of magnitude, it has little effect on the operation. Naturally occurring low levels of $C_n{}^2$ result in much smaller variances.
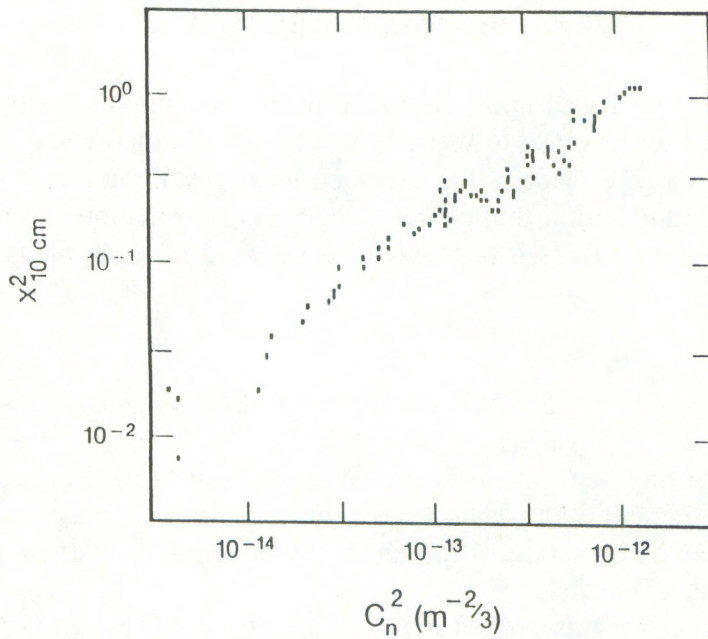
Figure 17. Mean-square signal fluctuations on a 500-m path using 10-cm-wavelength transmitting and receiving filters versus C_n^2 as measured by a separate incoherent-aperture scintillometer. No saturation is obvious.
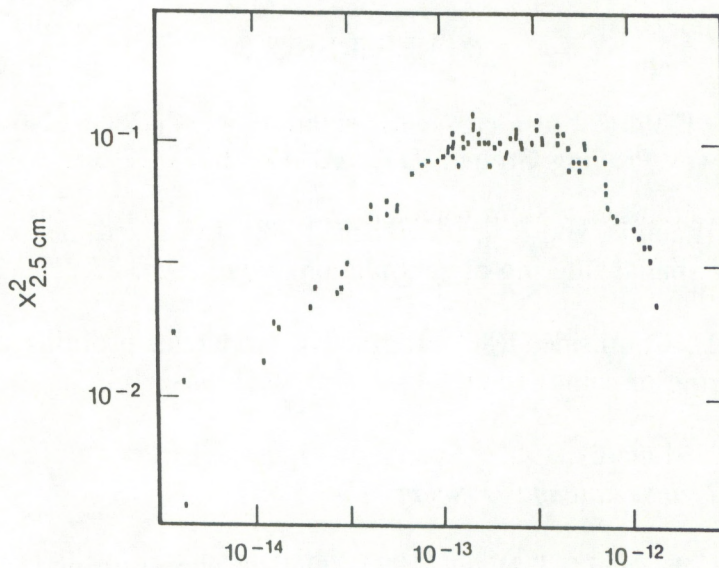

Figure 18. Mean-square signal fluctuations on a 500-m path using 2.5-cm wavelength transmitting and receiving filters versus C_n^2 as measured by a separate incoherent-aperture scintillometer. Note the large saturation effect at high turbulence levels.

4. CONCLUSIONS

A practical instrument, based upon the Lee profiling technique, has been constructed, and its performance in the field is close to that predicted from the theoretical analysis: the crosswind measurements take place at the expected locations along a 500-m optical path. Though the amplitude modulation that contains the wind information is very small, the co-variance analysis technique makes it possible to make wind measurements at C_n^2 levels as low as a few parts in 10^{-16}.

5. ACKNOWLEDGMENTS

6. REFERENCES

Bilthoft, C.A., 1988. Field test of a crosswind scintillometer. Report No. DPG-FR-88-317, U.S. Army Dugway Proving Ground, UT (AD:A200697), 12 pp.

Churnside, J.H., R.J. Lataitis, and R.S. Lawrence, 1988. Localized measurement of refractive turbulence using spatial filtering of scintillation. *Appl. Opt.* 27:2199-2213.

Clifford, S.F., and J.H. Churnside, 1987. Refractive turbulence profiling using synthetic aperture spatial filtering of scintillation. *Appl. Opt.* 26:1295-1303.

Clifford, S.F., and R.J. Lataitis, 1987. Spatial and temporal filtering of scintillation in remote sensing. *IEEE Trans. Antennas Propag.* AP-35:597-604.

Clifford, S.F., G.R. Ochs, and T.I. Wang, 1975. Optical wind sensing by observing the scintillations of a random scene. *Appl. Opt.* 14:2844-2850.

Hill, R.J., 1982. Theory of measuring the path-averaged inner scale of turbulence by spatial filtering of optical scintillations. *Appl. Opt.* 22:1201-1211.

Lataitis, R.J., R.S. Lawrence, S.F. Clifford, D.M. Farmer, and G.R. Ochs, 1986. Remote sensing using spatial filters: A case study. NOAA Tech. Memo. ERL WPL-140, NOAA Environmental Research Laboratories, Boulder, CO, 32 pp. (Available from the National Technical Information Service, 5285 Port Royal Rd., Springfield, VA 22161).

Lawrence, R.S., G.R. Ochs, and S.F. Clifford, 1972. Use of scintillations to measure average wind across a light beam. *Appl. Opt.* 11:239-243.

Lee, R.W., 1974. Remote probing using spatially filtered apertures. *J. Opt. Soc. Am.* 64:1295-1303.

Ochs, G.R., and W.D. Cartwright, 1980. Optical system Model IV for space-averaged wind and C_n^2 measurement. NOAA Tech. Memo. ERL WPL-52, NOAA Environmental Research Laboratories, Boulder, CO, 31 pp. (Available from the National Technical Information Service, 5285 Port Royal Rd., Springfield, VA 22161).

Ochs, G.R., and G.F. Miller, 1973. The NOAA optical system for measuring average wind. NOAA Tech. Memo. ERL WPL-9, NOAA Environmental Research Laboratories, Boulder, CO, 27 pp. (Available from the National Technical Information Service, 5285 Port Royal Rd., Springfield, VA 22161).

Ochs, G.R., and T.I. Wang, 1978. Finite aperture optical scintillometer for profiling wind and C_n^2. *Appl. Opt.* 17:3774-3778.

Ochs, G.R., S.F. Clifford, and T.I. Wang, 1976a. Laser wind sensing: The effects of saturation of scintillation. *Appl. Opt.* 15:403-408.

Ochs, G.R., T.I. Wang, R.S. Lawrence, and S.F. Clifford, 1976b. Refractive-turbulence profiles measured by one-dimensional spatial filtering of scintillation. *Appl. Opt.* 15:2504-2510.

Ochs, G.R., J.J. Wilson, S. Abbott, and R. George, 1988. Crosswind profiler Model II. NOAA Tech. Memo. ERL WPL-152, NOAA Environmental Research Laboratories, Boulder, CO, 56 pp. (Available from the National Technical Information Service, 5285 Port Royal Rd., Springfield, VA 22161).

Tatarskii, V.I., 1971. *The Effects of Atmospheric Turbulence on Wave Propagation.* Israel Program for Scientific Translations, Jerusalem, 472 pp.

Wang, T.I., and C.A. Bilthoft, 1991. A long-range scintillometer for remote wind and refractive index profiling. Proceedings, Seventh Symposium on Meteorological Observations and Instrumentation (71st Annual Meeting), New Orleans, Louisiana, 13-18 January 1991. American Meteorological Society, Boston, MA, 121-124.

Wang, T.I., S.F. Clifford, and G.R. Ochs, 1974. Wind and refractive-turbulence sensing using crossed laser beams. *Appl. Opt.* 13:2602-2603.

Wang, T.I., G.R. Ochs, and R.S. Lawrence, 1981. Wind measurements by temporal cross-correlations of the optical scintillations. *Appl. Opt.* 20:4073-4081.

APPENDIX

The spatially filtered covariance will have the approximate form

$$C_f(\rho_x, \tau) \propto \cos(\omega_0 \tau + \phi) \,, \tag{A1}$$

where ϕ depends on the separation ρ_x of the two receiving filters. The corresponding filtered cospectrum is given by

$$S_f(\rho_x, \omega) \propto e^{i\phi} \delta(\omega - \omega_0) + e^{-i\phi} \delta(\omega + \omega_0) \,, \tag{A2}$$

where δ is the Dirac delta function. The mean frequency $\tilde{\omega}$ of the covariance can then be expressed in terms of a first moment calculation:

$$\tilde{\omega} = \frac{\displaystyle\int_0^\infty d\omega\, \omega\, S_f(\rho_x, \omega)}{\displaystyle\int_0^\infty d\omega\, S_f(\rho_x, \omega)} \,, \tag{A3}$$

where the negative frequency part of the cospectrum has been neglected. This definition for the mean frequency is difficult to formulate using the expression for the covariance given in (5). We note, however, that in choosing the distance between spatial filters to be one-quarter of their spatial wavelength we have essentially set $\phi = \pi/2$ and the cospectrum is purely imaginary. We can then approximate (A3) by

$$\tilde{\omega} \approx \frac{Im\left\{\displaystyle\int_0^\infty d\omega\, \omega\, S_f(\rho_x, \omega)\right\}}{Im\left\{\displaystyle\int_0^\infty d\omega\, S_f(\rho_x, \omega)\right\}} \,. \tag{A4}$$